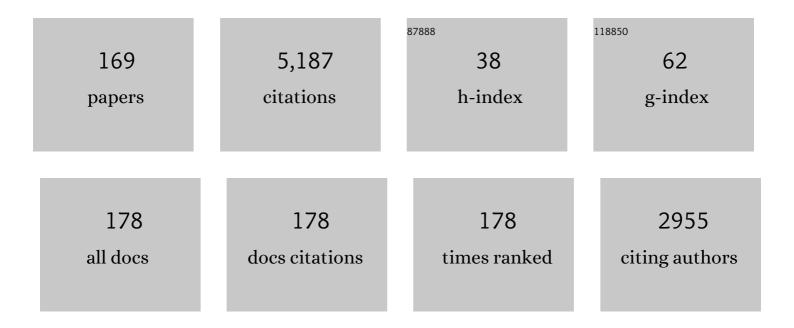
List of Publications by Year in descending order

Source: https://exaly.com/author-pdf/9371954/publications.pdf Version: 2024-02-01



#	Article	IF	CITATIONS
1	Resolving 3-D Mining Displacements From Multi-Track InSAR by Incorporating With a Prior Model: The Dynamic Changes and Adaptive Estimation of the Model Parameters. IEEE Transactions on Geoscience and Remote Sensing, 2022, 60, 1-10.	6.3	3
2	Prediction of Mining-Induced Kinematic 3-D Displacements From InSAR Using a Weibull Model and a Kalman Filter. IEEE Transactions on Geoscience and Remote Sensing, 2022, 60, 1-12.	6.3	6
3	A Phase Optimization Method for DS-InSAR Based on SKP Decomposition From Quad-Polarized Data. IEEE Geoscience and Remote Sensing Letters, 2022, 19, 1-5.	3.1	6
4	Retrieving the displacements of the Hutubi (China) underground gas storage during 2003–2020 from multi-track InSAR. Remote Sensing of Environment, 2022, 268, 112768.	11.0	14
5	Dynamic Estimation of Multi-Dimensional Deformation Time Series From InSAR Based on Kalman Filter and Strain Model. IEEE Transactions on Geoscience and Remote Sensing, 2022, 60, 1-16.	6.3	4
6	Surface Displacement and Source Model Separation of the Two Strongest Earthquakes During the 2019 Ridgecrest Sequence: Insights From InSAR, GPS, and Optical Data. Journal of Geophysical Research: Solid Earth, 2022, 127, .	3.4	8
7	Mitigation of time-series InSAR turbulent atmospheric phase noise: A review. Geodesy and Geodynamics, 2022, 13, 93-103.	2.2	8
8	Complete three-dimensional coseismic displacements due to the 2021 Maduo earthquake in Qinghai Province, China from Sentinel-1 and ALOS-2 SAR images. Science China Earth Sciences, 2022, 65, 687-697.	5.2	27
9	Three-Dimensional Surface Displacements of the 8 January 2022 Mw6.7 Menyuan Earthquake, China from Sentinel-1 and ALOS-2 SAR Observations. Remote Sensing, 2022, 14, 1404.	4.0	19
10	Review of the SBAS InSAR Time-series algorithms, applications, and challenges. Geodesy and Geodynamics, 2022, 13, 114-126.	2.2	61
11	Evolution of geodetic mass balance over the largest lake-terminating glacier in the Tibetan Plateau with a revised radar penetration depth based on multi-source high-resolution satellite data. Remote Sensing of Environment, 2022, 275, 113029.	11.0	3
12	Settlement Prediction of Reclaimed Coastal Airports with InSAR Observation: A Case Study of the Xiamen Xiang'an International Airport, China. Remote Sensing, 2022, 14, 3081.	4.0	4
13	Displacement history and potential triggering factors of Baige landslides, China revealed by optical imagery time series. Remote Sensing of Environment, 2021, 254, 112253.	11.0	23
14	Derivation of high-quality three-dimensional surface deformation velocities through multi-source point cloud fusion: Application to Kīlauea volcano. International Journal of Applied Earth Observation and Geoinformation, 2021, 95, 102270.	2.8	4
15	Monitoring Bridge Vibrations Based on GBSAR and Validation by High-Rate GPS Measurements. IEEE Journal of Selected Topics in Applied Earth Observations and Remote Sensing, 2021, 14, 5572-5580.	4.9	4
16	Correction of Time-Varying Baseline Errors Based on Multibaseline Airborne Interferometric Data Without High-Precision DEMs. IEEE Transactions on Geoscience and Remote Sensing, 2021, 59, 9307-9318.	6.3	8
17	Highâ€Resolution Water Vapor Maps Obtained by Merging Interferometric Synthetic Aperture Radar and GPS Measurements. Journal of Geophysical Research D: Atmospheres, 2021, 126, .	3.3	6
18	Mapping Complete Three-Dimensional Ice Velocities by Integrating Multi-Baseline and Multi-Aperture InSAR Measurements: A Case Study of the Grove Mountains Area, East Antarctic. Remote Sensing, 2021, 13, 643.	4.0	8

#	Article	IF	CITATIONS
19	Estimating three-dimensional coseismic deformations with the SM-VCE method based on heterogeneous SAR observations: Selection of homogeneous points and analysis of observation combinations. Remote Sensing of Environment, 2021, 255, 112298.	11.0	31
20	An Improved Quadtree Sampling Method for InSAR Seismic Deformation Inversion. Remote Sensing, 2021, 13, 1678.	4.0	9
21	Advanced InSAR Tropospheric Corrections From Global Atmospheric Models that Incorporate Spatial Stochastic Properties of the Troposphere. Journal of Geophysical Research: Solid Earth, 2021, 126, e2020JB020952.	3.4	22
22	Estimation of subcanopy topography based on single-baseline TanDEM-X InSAR data. Journal of Geodesy, 2021, 95, 1.	3.6	9
23	A Strainâ€Model Based InSAR Time Series Method and Its Application to The Geysers Geothermal Field, California. Journal of Geophysical Research: Solid Earth, 2021, 126, e2021JB021939.	3.4	11
24	Continued Monitoring and Modeling of Xingfeng Solid Waste Landfill Settlement, China, Based on Multiplatform SAR Images. Remote Sensing, 2021, 13, 3286.	4.0	2
25	An Improved Method for Automatic Identification and Assessment of Potential Geohazards Based on MT-InSAR Measurements. Remote Sensing, 2021, 13, 3490.	4.0	14
26	Block PS-InSAR ground deformation estimation for large-scale areas based on network adjustment. Journal of Geodesy, 2021, 95, 1.	3.6	7
27	Orbit error removal in InSAR/MTInSAR with a patch-based polynomial model. International Journal of Applied Earth Observation and Geoinformation, 2021, 102, 102438.	2.8	6
28	The joint driving effects of climate and weather changes caused the Chamoli glacier-rock avalanche in the high altitudes of the India Himalaya. Science China Earth Sciences, 2021, 64, 1909-1921.	5.2	20
29	An Improved Phase Unwrapping Method Based on Hierarchical Networking and Constrained Adjustment. Remote Sensing, 2021, 13, 4193.	4.0	6
30	Coseismic and Early Postseismic Slip Models of the 2021 Mw 7.4 Maduo Earthquake (Western China) Estimated by Spaceâ€Based Geodetic Data. Geophysical Research Letters, 2021, 48, .	4.0	36
31	CRInSAR Using Two-Step LAMBDA Algorithm for Nonlinear Deformation Estimation: Case Study of Monitoring Xiangtan Converter Station, China. IEEE Geoscience and Remote Sensing Letters, 2020, 17, 963-967.	3.1	6
32	Quantifying the spatio-temporal patterns of dune migration near Minqin Oasis in northwestern China with time series of Landsat-8 and Sentinel-2 observations. Remote Sensing of Environment, 2020, 236, 111498.	11.0	29
33	Kinematic Coregistration of Sentinel-1 TOPSAR Images Based on Sequential Least Squares Adjustment. IEEE Journal of Selected Topics in Applied Earth Observations and Remote Sensing, 2020, 13, 3083-3093.	4.9	12
34	A New Weighting Method by Considering the Physical Characteristics of Atmospheric Turbulence and Decorrelation Noise in SBAS-InSAR. Remote Sensing, 2020, 12, 2557.	4.0	14
35	Pre- and post-failure spatial-temporal deformation pattern of the Baige landslide retrieved from multiple radar and optical satellite images. Engineering Geology, 2020, 279, 105880.	6.3	46
36	The Surge of the Hispar Glacier, Central Karakoram: SAR 3â€Ð Flow Velocity Time Series and Thickness Changes. Journal of Geophysical Research: Solid Earth, 2020, 125, e2019JB018945.	3.4	19

#	Article	IF	CITATIONS
37	Adaptively Selecting Interferograms for SBAS-InSAR Based on Graph Theory and Turbulence Atmosphere. IEEE Access, 2020, 8, 112898-112909.	4.2	6
38	Investigating the Recent Surge in the Monomah Glacier, Central Kunlun Mountain Range with Multiple Sources of Remote Sensing Data. Remote Sensing, 2020, 12, 966.	4.0	12
39	SAR Interferometric Baseline Refinement Based on Flat-Earth Phase without a Ground Control Point. Remote Sensing, 2020, 12, 233.	4.0	14
40	Non-differential water vapor estimation from SBAS-InSAR. Journal of Atmospheric and Solar-Terrestrial Physics, 2020, 204, 105284.	1.6	4
41	Understanding Land Subsidence Along the Coastal Areas of Guangdong, China, by Analyzing Multi-Track MTInSAR Data. Remote Sensing, 2020, 12, 299.	4.0	25
42	Use of SAR/InSAR in Mining Deformation Monitoring, Parameter Inversion, and Forward Predictions: A Review. IEEE Geoscience and Remote Sensing Magazine, 2020, 8, 71-90.	9.6	72
43	Fusing adjacent-track InSAR datasets to densify the temporal resolution of time-series 3-D displacement estimation over mining areas with a prior deformation model and a generalized weighting least-squares method. Journal of Geodesy, 2020, 94, 1.	3.6	11
44	Change detection, risk assessment and mass balance of mobile dune fields near Dunhuang Oasis with optical imagery and global terrain datasets. International Journal of Digital Earth, 2020, 13, 1604-1623.	3.9	6
45	Surface deformation evolution in the Pearl River Delta between 2006 and 2011 derived from the ALOS1/PALSAR images. Earth, Planets and Space, 2020, 72, .	2.5	7
46	An Optimized Choice of UCPML to Truncate Lattices With Rotated Staggered Grid Scheme for Ground Penetrating Radar Simulation. IEEE Transactions on Geoscience and Remote Sensing, 2019, 57, 8695-8706.	6.3	12
47	Complete Threeâ€Dimensional Coseismic Deformation Field of the 2016 Central Tottori Earthquake by Integrating Left―and Rightâ€Looking InSAR Observations With the Improved SMâ€VCE Method. Journal of Geophysical Research: Solid Earth, 2019, 124, 12099-12115.	3.4	27
48	Source parameters and slip distribution of the 2018 M 7.5 Palu, Indonesia earthquake estimated from space-based geodesy. Tectonophysics, 2019, 772, 228216.	2.2	27
49	Spatially Heterogeneous Land Surface Deformation Data Fusion Method Based on an Enhanced Spatio-Temporal Random Effect Model. Remote Sensing, 2019, 11, 1084.	4.0	8
50	A Novel Vessel Velocity Estimation Method Using Dual-Platform TerraSAR-X and TanDEM-X Full Polarimetric SAR Data in Pursuit Monostatic Mode. IEEE Transactions on Geoscience and Remote Sensing, 2019, 57, 6130-6144.	6.3	9
51	Geodetic glacier mass balance (1975–1999) in the central Pamir using the SRTM DEM and KH-9 imagery. Journal of Glaciology, 2019, 65, 309-320.	2.2	20
52	Monitoring the Degradation of Island Permafrost Using Time-Series InSAR Technique: A Case Study of Heihe, China. Sensors, 2019, 19, 1364.	3.8	15
53	Time-series InSAR ground deformation monitoring: Atmospheric delay modeling and estimating. Earth-Science Reviews, 2019, 192, 258-284.	9.1	78
54	Mapping ground displacement by a multiple phase difference-based InSAR approach: with stochastic model estimation and turbulent troposphere mitigation. Journal of Geodesy, 2019, 93, 1313-1333.	3.6	7

#	Article	IF	CITATIONS
55	Anisotropy of atmospheric delay in InSAR and its effect on InSAR atmospheric correction. Journal of Geodesy, 2019, 93, 241-265.	3.6	12
56	Quantifying Dynamic Characteristics of Dune Migration in Northwestern China with Multitemporal Optical Satellite Observations. , 2019, , .		1
57	A Block Ramp Errors Correction Method of Planet Subpixel Offset: Application to the 2018 Mw 7.5 Palu Earthquake, Indonesia. IEEE Access, 2019, 7, 174924-174931.	4.2	5
58	A Method for Surface Water Body Detection and DEM Generation With Multigeometry TanDEM-X Data. IEEE Journal of Selected Topics in Applied Earth Observations and Remote Sensing, 2019, 12, 151-161.	4.9	8
59	Quantifying glacier mass change and its contribution to lake growths in central Kunlun during 2000–2015 from multi-source remote sensing data. Journal of Hydrology, 2019, 570, 38-50.	5.4	47
60	A Method for Measuring 3-D Surface Deformations With InSAR Based on Strain Model and Variance Component Estimation. IEEE Transactions on Geoscience and Remote Sensing, 2018, 56, 239-250.	6.3	48
61	An InSAR-Based Temporal Probability Integral Method and its Application for Predicting Mining-Induced Dynamic Deformations and Assessing Progressive Damage to Surface Buildings. IEEE Journal of Selected Topics in Applied Earth Observations and Remote Sensing, 2018, 11, 472-484.	4.9	28
62	Deriving a time series of 3D glacier motion to investigate interactions of a large mountain glacial system with its glacial lake: Use of Synthetic Aperture Radar Pixel Offset-Small Baseline Subset technique. Journal of Hydrology, 2018, 559, 596-608.	5.4	27
63	Transpressional Rupture Cascade of the 2016 M _w 7.8 Kaikoura Earthquake, New Zealand. Journal of Geophysical Research: Solid Earth, 2018, 123, 2396-2409.	3.4	83
64	Time-Series 3-D Mining-Induced Large Displacement Modeling and Robust Estimation From a Single-Geometry SAR Amplitude Data Set. IEEE Transactions on Geoscience and Remote Sensing, 2018, 56, 3600-3610.	6.3	16
65	An Alternative Method for Estimating 3-D Large Displacements of Mining Areas from a Single SAR Amplitude Pair Using Offset Tracking. IEEE Transactions on Geoscience and Remote Sensing, 2018, 56, 3645-3656.	6.3	18
66	Glacier mass balance in the Qinghai–Tibet Plateau and its surroundings from the mid-1970s to 2000 based on Hexagon KH-9 and SRTM DEMs. Remote Sensing of Environment, 2018, 210, 96-112.	11.0	147
67	Underlying topography extraction over forest areas from multi-baseline PolInSAR data. Journal of Geodesy, 2018, 92, 727-741.	3.6	10
68	Stochastic modeling for time series InSAR: with emphasis on atmospheric effects. Journal of Geodesy, 2018, 92, 185-204.	3.6	35
69	A new moving model test method for the measurement of aerodynamic drag coefficient of high-speed trains based on machine vision. Proceedings of the Institution of Mechanical Engineers, Part F: Journal of Rail and Rapid Transit, 2018, 232, 1425-1436.	2.0	6
70	Locating and defining underground goaf caused by coal mining from space-borne SAR interferometry. ISPRS Journal of Photogrammetry and Remote Sensing, 2018, 135, 112-126.	11.1	43
71	Deriving time-series three-dimensional displacements of mining areas from a single-geometry InSAR dataset. Journal of Geodesy, 2018, 92, 529-544.	3.6	31
72	High-Resolution Three-Dimensional Displacement Retrieval of Mining Areas From a Single SAR Amplitude Pair Using the SPIKE Algorithm. IEEE Journal of Selected Topics in Applied Earth Observations and Remote Sensing, 2018, 11, 3782-3793.	4.9	8

#	Article	IF	CITATIONS
73	Anomalous Glacier Changes in the Southeast of Tuomuerâ€Khan Tengri Mountain Ranges, Central Tianshan. Journal of Geophysical Research D: Atmospheres, 2018, 123, 6840-6863.	3.3	11
74	Source parameters and triggering links of the earthquake sequence in central Italy from 2009 to 2016 analyzed with GPS and InSAR data. Tectonophysics, 2018, 744, 285-295.	2.2	29
75	Kinematic Parameter Inversion of the Slumgullion Landslide Using the Time Series Offset Tracking Method With UAVSAR Data. Journal of Geophysical Research: Solid Earth, 2018, 123, 8110-8124.	3.4	18
76	Mapping three-dimensional co-seismic surface deformations associated with the 2015 MW7.2 Murghab earthquake based on InSAR and characteristics of crustal strain. Science China Earth Sciences, 2018, 61, 1451-1466.	5.2	8
77	Toward full exploitation of coherent and incoherent information in Sentinelâ€1 TOPS data for retrieving surface displacement: Application to the 2016 Kumamoto (Japan) earthquake. Geophysical Research Letters, 2017, 44, 1758-1767.	4.0	68
78	The potential of more accurate InSAR covariance matrix estimation for land cover mapping. ISPRS Journal of Photogrammetry and Remote Sensing, 2017, 126, 120-128.	11.1	30
79	Slight glacier mass loss in the Karakoram region during the 1970s to 2000 revealed by KH-9 images and SRTM DEM. Journal of Glaciology, 2017, 63, 331-342.	2.2	96
80	Early 21st century glacier thickness changes in the Central Tien Shan. Remote Sensing of Environment, 2017, 192, 12-29.	11.0	42
81	An Extension of the InSAR-Based Probability Integral Method and Its Application for Predicting 3-D Mining-Induced Displacements Under Different Extraction Conditions. IEEE Transactions on Geoscience and Remote Sensing, 2017, 55, 3835-3845.	6.3	38
82	Which Fault Segments Ruptured in the 2008 Wenchuan Earthquake and Which Did Not? New Evidence from Nearâ€Fault 3D Surface Displacements Derived from SAR Image Offsets. Bulletin of the Seismological Society of America, 2017, 107, 1185-1200.	2.3	29
83	Estimation of 3-D Surface Displacement Based on InSAR and Deformation Modeling. IEEE Transactions on Geoscience and Remote Sensing, 2017, 55, 2007-2016.	6.3	20
84	Potential of geosynchronous SAR interferometric measurements in estimating three-dimensional surface displacements. Science China Information Sciences, 2017, 60, 1.	4.3	21
85	On the Accuracy of Topographic Residuals Retrieved by MTInSAR. IEEE Transactions on Geoscience and Remote Sensing, 2017, 55, 1053-1065.	6.3	31
86	Deriving Dynamic Subsidence of Coal Mining Areas Using InSAR and Logistic Model. Remote Sensing, 2017, 9, 125.	4.0	92
87	Retrieving 3-D Large Displacements of Mining Areas from a Single Amplitude Pair of SAR Using Offset Tracking. Remote Sensing, 2017, 9, 338.	4.0	34
88	Recent Landslide Movement in Tsaoling, Taiwan Tracked by TerraSAR-X/TanDEM-X DEM Time Series. Remote Sensing, 2017, 9, 353.	4.0	27
89	High-Rise Building Layover Exploitation with Non-Local Frequency Estimation in SAR Interferograms. Remote Sensing, 2017, 9, 579.	4.0	4
90	Deriving Spatio-Temporal Development of Ground Subsidence Due to Subway Construction and Operation in Delta Regions with PS-InSAR Data: A Case Study in Guangzhou, China. Remote Sensing, 2017, 9, 1004.	4.0	55

#	Article	IF	CITATIONS
91	Subsidence Evolution of the Leizhou Peninsula, China, Based on InSAR Observation from 1992 to 2010. Applied Sciences (Switzerland), 2017, 7, 466.	2.5	13
92	Effects of External Digital Elevation Model Inaccuracy on StaMPS-PS Processing: A Case Study in Shenzhen, China. Remote Sensing, 2017, 9, 1115.	4.0	17
93	Deriving 3-D Time-Series Ground Deformations Induced by Underground Fluid Flows with InSAR: Case Study of Sebei Gas Fields, China. Remote Sensing, 2017, 9, 1129.	4.0	7
94	Investigating the Ground Deformation and Source Model of the Yangbajing Geothermal Field in Tibet, China with the WLS InSAR Technique. Remote Sensing, 2016, 8, 191.	4.0	26
95	Continent-Wide 2-D Co-Seismic Deformation of the 2015 Mw 8.3 Illapel, Chile Earthquake Derived from Sentinel-1A Data: Correction of Azimuth Co-Registration Error. Remote Sensing, 2016, 8, 376.	4.0	18
96	Coastal Subsidence Monitoring Associated with Land Reclamation Using the Point Target Based SBAS-InSAR Method: A Case Study of Shenzhen, China. Remote Sensing, 2016, 8, 652.	4.0	78
97	Spatio-Temporal Error Sources Analysis and Accuracy Improvement in Landsat 8 Image Ground Displacement Measurements. Remote Sensing, 2016, 8, 937.	4.0	32
98	Coseismic Deformation of the 2015 <i>M</i> _w Â6.4 Pishan, China, Earthquake Estimated from Sentinelâ€IA and ALOS2 Data. Seismological Research Letters, 2016, 87, 800-806.	1.9	20
99	Vertical and horizontal displacements of Los Angeles from InSAR and GPS time series analysis: Resolving tectonic and anthropogenic motions. Journal of Geodynamics, 2016, 99, 27-38.	1.6	35
100	An improved geodetic source model for the 1999 <i>M</i> _w 6.3 Chamoli earthquake, India. Geophysical Journal International, 2016, 205, 236-242.	2.4	28
101	Monitoring surface deformation over permafrost with an improved SBAS-InSAR algorithm: With emphasis on climatic factors modeling. Remote Sensing of Environment, 2016, 184, 276-287.	11.0	131
102	Blind thrust rupture of the 2015 Mw 6.4 Pishan earthquake in the Northwest Tibetan Plateau by joint inversion of InSAR and seismic data. Journal of Asian Earth Sciences, 2016, 132, 118-128.	2.3	7
103	The 3-D surface deformation, coseismic fault slip and after-slip of the 2010 Mw6.9 Yushu earthquake, Tibet, China. Journal of Asian Earth Sciences, 2016, 124, 260-268.	2.3	11
104	InSAR-Based Model Parameter Estimation of Probability Integral Method and Its Application for Predicting Mining-Induced Horizontal and Vertical Displacements. IEEE Transactions on Geoscience and Remote Sensing, 2016, 54, 4818-4832.	6.3	64
105	InSAR analysis of surface deformation over permafrost to estimate active layer thickness based on one-dimensional heat transfer model of soils. Scientific Reports, 2015, 5, 15542.	3.3	66
106	Improved fast mean shift algorithm for remote sensing image segmentation. IET Image Processing, 2015, 9, 389-394.	2.5	8
107	Crosswind stability of high-speed trains in special cuts. Journal of Central South University, 2015, 22, 2849-2856.	3.0	27
108	Retrieving three-dimensional displacement fields of mining areas from a single InSAR pair. Journal of Geodesy, 2015, 89, 17-32.	3.6	84

#	Article	IF	CITATIONS
109	Monitoring the land subsidence with persistent scatterer interferometry in Nansha District, Guangdong, China. Natural Hazards, 2015, 75, 2947-2964.	3.4	18
110	Source parameters of the 2014 Mw 6.1 South Napa earthquake estimated from the Sentinel 1A, COSMO-SkyMed and GPS data. Tectonophysics, 2015, 655, 139-146.	2.2	32
111	Characterizing sudden geo-hazards in mountainous areas by D-InSAR with an enhancement of topographic error correction. Natural Hazards, 2015, 75, 2343-2356.	3.4	13
112	Geodetic model of the 2015 April 25 Mw 7.8 Gorkha Nepal Earthquake and Mw 7.3 aftershock estimated from InSAR and GPS data. Geophysical Journal International, 2015, 203, 896-900.	2.4	71
113	Slope deformation prior to Zhouqu, China landslide from InSAR time series analysis. Remote Sensing of Environment, 2015, 156, 45-57.	11.0	148
114	A novel method for determining the anisotropy of geophysical parameters: unit range variation increment (URVI). Applied Geophysics, 2014, 11, 340-349.	0.6	4
115	Spatial statistics of atmospheric signal in repeat-pass InSAR. , 2014, , .		0
116	Generalized functional model of maximum and minimum detectable deformation gradient for PALSAR interferometry. Transactions of Nonferrous Metals Society of China, 2014, 24, 824-832.	4.2	7
117	Resolving three-dimensional surface displacements from InSAR measurements: A review. Earth-Science Reviews, 2014, 133, 1-17.	9.1	361
118	A Refined Strategy for Removing Composite Errors of SAR Interferogram. IEEE Geoscience and Remote Sensing Letters, 2014, 11, 143-147.	3.1	45
119	InSAR Coherence Estimation for Small Data Sets and Its Impact on Temporal Decorrelation Extraction. IEEE Transactions on Geoscience and Remote Sensing, 2014, 52, 6584-6596.	6.3	24
120	Hybrid Approach for Unbiased Coherence Estimation for Multitemporal InSAR. IEEE Transactions on Geoscience and Remote Sensing, 2014, 52, 2459-2473.	6.3	59
121	The Improvement for Baran Phase Filter Derived From Unbiased InSAR Coherence. IEEE Journal of Selected Topics in Applied Earth Observations and Remote Sensing, 2014, 7, 3002-3010.	4.9	18
122	Investigating mountain glacier motion with the method of SAR intensity-tracking: Removal of topographic effects and analysis of the dynamic patterns. Earth-Science Reviews, 2014, 138, 179-195.	9.1	37
123	A Novel Multitemporal InSAR Model for Joint Estimation of Deformation Rates and Orbital Errors. IEEE Transactions on Geoscience and Remote Sensing, 2014, 52, 3529-3540.	6.3	77
124	Retrieving three-dimensional coseismic displacements of the 2008 Gaize, Tibet earthquake from multi-path interferometric phase analysis. Natural Hazards, 2014, 73, 1311-1322.	3.4	12
125	3-D movement mapping of the alpine glacier in Qinghai-Tibetan Plateau by integrating D-InSAR, MAI and Offset-Tracking: Case study of the Dongkemadi Glacier. Global and Planetary Change, 2014, 118, 62-68.	3.5	48
126	Monitoring of Surface Subsidence of the Mining Area Based on SBAS. Journal of Computers, 2014, 9, .	0.4	2

#	Article	IF	CITATIONS
127	Improved Goldstein filter for InSAR noise reduction based on local SNR. Journal of Central South University, 2013, 20, 1896-1903.	3.0	13
128	Spatial–temporal surface deformation of Los Angeles over 2003–2007 from weighted least squares DInSAR. International Journal of Applied Earth Observation and Geoinformation, 2013, 21, 484-492.	2.8	20
129	Deriving surface motion of mountain glaciers in the Tuomuer-Khan Tengri Mountain Ranges from PALSAR images. Global and Planetary Change, 2013, 101, 61-71.	3.5	19
130	Kalman-Filter-Based Approach for Multisensor, Multitrack, and Multitemporal InSAR. IEEE Transactions on Geoscience and Remote Sensing, 2013, 51, 4226-4239.	6.3	53
131	Derivation of 3-D coseismic surface displacement fields for the 2011 Mw 9.0 Tohoku-Oki earthquake from InSAR and GPS measurements. Geophysical Journal International, 2013, 192, 573-585.	2.4	27
132	Shortcomings of InSAR for studying megathrust earthquakes: The case of the M _w 9.0 Tohokuâ€Oki earthquake. Geophysical Research Letters, 2012, 39, .	4.0	22
133	Three-Dimensional Surface Displacements From InSAR and GPS Measurements With Variance Component Estimation. IEEE Geoscience and Remote Sensing Letters, 2012, 9, 754-758.	3.1	62
134	Mapping ground surface deformation using temporarily coherent point SAR interferometry: Application to Los Angeles Basin. Remote Sensing of Environment, 2012, 117, 429-439.	11.0	164
135	Correcting ionospheric effects and monitoring two-dimensional displacement fields with multiple-aperture InSAR technology with application to the Yushu earthquake. Science China Earth Sciences, 2012, 55, 1961-1971.	5.2	26
136	3D coseismic Displacement of 2010 Darfield, New Zealand earthquake estimated from multi-aperture InSAR and D-InSAR measurements. Journal of Geodesy, 2012, 86, 1029-1041.	3.6	95
137	Correcting atmospheric effects on InSAR with MERIS water vapour data and elevation-dependent interpolation model. Geophysical Journal International, 2012, 189, 898-910.	2.4	60
138	Calibration of an InSAR-Derived Coseimic Deformation Map Associated With the 2011 Mw-9.0 Tohoku-Oki Earthquake. IEEE Geoscience and Remote Sensing Letters, 2012, 9, 302-306.	3.1	39
139	Coseismic slip distribution of 2009 L'Aquila earthquake derived from InSAR and GPS data. Journal of Central South University, 2012, 19, 244-251.	3.0	8
140	Modeling minimum and maximum detectable deformation gradients of interferometric SAR measurements. International Journal of Applied Earth Observation and Geoinformation, 2011, 13, 766-777.	2.8	39
141	Interpolating atmospheric water vapor delay by incorporating terrain elevation information. Journal of Geodesy, 2011, 85, 555-564.	3.6	30
142	Discussion on GPS-RTK Using in Undersea Topographic Survey. Key Engineering Materials, 2011, 467-469, 829-834.	0.4	1
143	Inferring three-dimensional surface displacement field by combining SAR interferometric phase and amplitude information of ascending and descending orbits. Science China Earth Sciences, 2010, 53, 550-560.	5.2	48
144	The least-squares estimation of adjustment model constrained by some non-negative parameters. Survey Review, 2010, 42, 62-71.	1.2	7

#	Article	IF	CITATIONS
145	Coseismic fault slip of the 2008 M _w 7.9 Wenchuan earthquake estimated from InSAR and GPS measurements. Geophysical Research Letters, 2010, 37, .	4.0	94
146	Improved filtering parameter determination for the Goldstein radar interferogram filter. ISPRS Journal of Photogrammetry and Remote Sensing, 2008, 63, 621-634.	11.1	83
147	Two-dimensional Co-Seismic Surface Displacements Field of the Chi-Chi Earthquake Inferred from SAR Image Matching. Sensors, 2008, 8, 6484-6495.	3.8	20
148	Least Squares-Based Filter for Remote SensingImage Noise Reduction. IEEE Transactions on Geoscience and Remote Sensing, 2008, 46, 2044-2049.	6.3	41
149	Comparative Study of Empirical Tropospheric Models for the Hong Kong Region. Survey Review, 2008, 40, 328-341.	1.2	8
150	Atmospheric Effects on InSAR Measurements and Their Mitigation. Sensors, 2008, 8, 5426-5448.	3.8	139
151	Helmert Variance Component Estimation-based Vondrak Filter and its Application in GPS Multipath Error Mitigation. , 2008, , 287-292.		4
152	Six years of land subsidence in shanghai revealed by JERS-1 SAR data. , 2007, , .		6
153	Study on Ocean Wind Vector Retrieval from ERSâ€2 SAR Image. Chinese Journal of Geophysics, 2007, 50, 1466-1473.	0.2	3
154	Atmospheric effects on repeat-pass InSAR measurements over Shanghai region. Journal of Atmospheric and Solar-Terrestrial Physics, 2007, 69, 1344-1356.	1.6	28
155	Filtering method for SAR interferograms with strong noise. International Journal of Remote Sensing, 2006, 27, 2991-3000.	2.9	15
156	Modeling of atmospheric effects on InSAR measurements by incorporating terrain elevation information. Journal of Atmospheric and Solar-Terrestrial Physics, 2006, 68, 1189-1194.	1.6	37
157	Hazard development mechanism and deformation estimation of water solution mining area. Central South University, 2006, 13, 738-742.	0.5	2
158	Quantitative study of atmospheric effects in spaceborne InSAR measurements. Central South University, 2005, 12, 494-498.	0.5	6
159	Pre- and co-seismic ground deformations of the 1999 Chi-Chi, Taiwan earthquake, measured with SAR interferometry. Computers and Geosciences, 2004, 30, 333-343.	4.2	26
160	Modeling atmospheric effects on InSAR with meteorological and continuous GPS observations: algorithms and some test results. Journal of Atmospheric and Solar-Terrestrial Physics, 2004, 66, 907-917.	1.6	47
161	Ground Subsidence Monitoring in Hong Kong with Satellite SAR Interferometry. Photogrammetric Engineering and Remote Sensing, 2004, 70, 1151-1156.	0.6	93
162	SCGM(1,m)c model with time-lag and its application in deformation analysis. Central South University, 2001, 8, 40-44.	0.5	1

#	Article	IF	CITATIONS
163	Ground settlement of Chek Lap Kok Airport, Hong Kong, detected by satellite synthetic aperture radar interferometry. Science Bulletin, 2001, 46, 1778-1782.	1.7	19
164	SAR interferogram filtering with 2D Vondrak filter. , 0, , .		3
165	Modeling of atmospheric effects on InSAR by incorporating terrain elevation information. , 0, , .		0
166	Magnitude and Extent of Six Years of Land Subsidence in Shanghai Revealed by JERS-1 SAR Data. , 0, , .		1
167	The Application of GPS Using in Steel Sheet Pile Implementing the Localization on the Sea Surveying. Advanced Materials Research, 0, 204-210, 741-745.	0.3	0
168	Analysis on the Application of GPS in Hull Installment and Marine Monitoring. Applied Mechanics and Materials, 0, 55-57, 1111-1115.	0.2	1
169	Investigating the bias of TanDEM-X digital elevation models of glaciers on the Tibetan Plateau: impacting factors and potential effects on geodetic mass-balance measurements. Journal of Glaciology, 0, , 1-14.	2.2	10